J. Synchrotron Rad. (1996). **3**, 239–244

Photoelectron Holography of the Si(001) Surface

T. Nakatani,[a] H. Nishimoto,[a] H. Daimon,[a] S. Suga,[a] H. Namba,[b] T. Ohta,[b] Y. Kagoshima[c] and T. Miyahara[b]

[a]Department of Material Physics, Faculty of Engineering Science, Osaka University, Toyonaka, Osaka 560, Japan, [b]Department of Chemistry, Faculty of Science, The University of Tokyo, Bunkyo-ku, Tokyo 113, Japan, and [c]Photon Factory, National Laboratory for High Energy Physics, Oho, Tsukuba, Ibaraki 305, Japan. E-mail: suga@mp.es.osaka-u.ac.jp

(*Received 26 February 1996; accepted 14 May 1996*)

Three-dimensional images of the near-surface atom arrangement were calculated from two-dimensional photoelectron diffraction data by several imaging algorithms: (i) a basic method with a Fourier transformation at one kinetic energy over **k** space, considering the phase factor due to the path-length difference; (ii) energy summation of the above results; (iii) Fourier transformation within small **k**-space windows; and (iv) their combinations. Atomic images produced by these methods from the experimental Si 2*p* photoelectron diffraction patterns of an Si(001) surface are compared with the crystal geometry. The results show that the energy-summed small-window method, called SWEEP, gives the best images.

Keywords: photoelectron holography; photoelectron diffraction; Si(001) surface.

1. Introduction

The analysis of photoelectron diffraction has so far required tedious trial-and-error calculations to simulate the experimental diffraction patterns. Szöke (1986) and Barton (1988), however, have suggested that Auger and photoelectron diffraction intensity maps can be used as holograms of the near-surface atomic geometry of single-crystal samples, and that such holograms can, in principle, be inverted to three-dimensional real-space images of surface atoms by two-dimensional Fourier transformation. This method is called 'photoelectron holography'.

The original idea of holography was proposed by Gabor (1948) and used as a method to reconstruct a three-dimensional image of a given object from a two-dimensional pattern which recorded the interference of the reference wave and of the wave scattered by the object. It is necessary in holography for the reference wave to be coherent. In visible-light holography, lasers have been conventionally used as coherent wave sources. In photoelectron holography on the other hand, the core-level photoelectron plays the role of the reference wave. When we use a photoelectron diffraction pattern as a hologram, we are able to reconstruct a local atomic geometry around one specific kind of atom near the crystal-surface region selected by using a specific feature in the photoelectron spectrum.

The reconstruction technique has been improved by several researchers: for example, Barton (1991) reduced multiple-scattering effects and twin images by the energy summation (ES) method, Huang, Li & Tong (1991) developed the small-window energy-extension process (SWEEP), Hardcastle *et al.* (1991) developed the scattered-wave included Fourier transformation (SWIFT), and Rous & Rubin (1994) proposed an algorithm based on the complete quantum mechanical treatment of the photoelectron propagation and scattering. Recently, Denecke, Eckstein, Ley, Bocquet & Leckey (1995) applied SWIFT to GaAs(001), and Roesler, Sieger, Miller & Chiang (1995) applied the ES method to Pb/Si(111)($\sqrt{3} \times \sqrt{3}$)$R30°$ – Ag.

One can easily obtain clean silicon surfaces by direct-current heating in ultra-high vacuum ($\sim 10^{-10}$ Torr). The silicon single-crystal has the diamond structure, which consists of two face-centred cubic sublattices. The Si(001) 1×1 surface is easily reconstructed to a 2×1 superstructure. The reconstructed structure has been analyzed by medium-energy ion scattering (MEIS) (Tromp, Smeenk & Saris, 1983), low-energy electron diffraction (LEED) (Holland, Duke & Paton, 1984) and surface core-level photoelectron diffraction (Bullock *et al.*, 1995).

In the present study we have measured two-dimensional diffraction patterns of Si 2*p* photoelectrons from an Si(001) surface. These patterns have been Fourier transformed by several methods and the results have been compared with the surface crystal geometry in order to test the validity of different photoelectron holography reconstruction methods.

2. Experimental

We have performed the measurement at the BL-7A beamline of the research centre of spectra chemistry of the University of Tokyo at the Photon Factory (a 2.5 GeV positron

storage ring) of the National Laboratory for High Energy Physics, Tsukuba. This beamline is a soft X-ray beamline (40–1000 eV) (Namba *et al.*, 1989) connected to a bending magnet. The direction of the synchrotron beam was normal to the sample surface. The polarization was in the horizontal direction. We have used a two-dimensional display-type spherical mirror analyzer (Daimon, 1988, 1990; Nishimoto *et al.*, 1993) which can record the two-dimensional angular distribution of energy-analyzed photoelectrons without distortion in a wide solid angle within $\pm 50^\circ$ simultaneously. The two-dimensional pattern projected onto a flat fluorescent screen is recorded as a digital image by a cooled CCD camera. The Si sample was cut from an Si(001) wafer (*n*-type, 2.99 Ω cm) to a size of $3 \times 10 \times 0.6$ mm^3. The sample was cleaned by repeated direct-current heating for 5 s up to 1523 K under a pressure of 2×10^{-10} Torr. The surface quality was confirmed by the observation of a clear 2×1 LEED pattern. First, we measured the angle-integrated photoelectron spectra and then adjusted the incident photon energy so that the Si 2*p* photoelectron kinetic energy was 350, 450 or 650 eV. Then we measured the photoelectron diffraction patterns at azimuthal angles φ of 0, 22.5 and 45°. Here, φ is defined as the angle between the [010] direction of the sample and the horizontal direction in Fig. 1. The pattern of the transmittance efficiency of the analyzer for each kinetic energy was evaluated by averaging the patterns for the three azimuthal angles.

3. Photoelectron diffraction

Figs. 1(*a*)–1(*c*) are the photoelectron diffraction patterns at kinetic energies of 350, 450 and 650 eV. We have marked the [112], [011] directions *etc.* in Fig. 1(*d*). The brighter regions correspond to stronger photoemission intensity. The centre of the picture is the surface-normal direction [001]. The edge of the picture corresponds to a polar angle θ of 47°. The patterns have been divided by the transmittance efficiency pattern whose evaluation is discussed above. The normalized photoelectron diffraction patterns were averaged utilizing the fourfold and the horizontal and vertical mirror symmetries of the Si(001) surface. With these symmetry operations we simulated the diffraction patterns produced by unpolarized light, although we used linearly polarized light. Note that the dependence on polarization is not essential in the holographic analysis except for the circularly polarized light. The polar angles of these pictures were re-scaled by multiplying the original values by $\cos\theta$ so that the horizontal and vertical scales are proportional to the k_x and k_y components of the photoelectron wavevector.

The high-intensity regions in Figs. 1(*a*)–1(*c*) are due to forward focusing. The forward-focusing features are induced by scattering of the outgoing photoelectrons along the directions of the nearest neighbour scatterers. When we measure a photoelectron diffraction pattern from atoms in a crystal, the high-intensity directions coincide with the axes along which atoms line up with high density. Hence, we

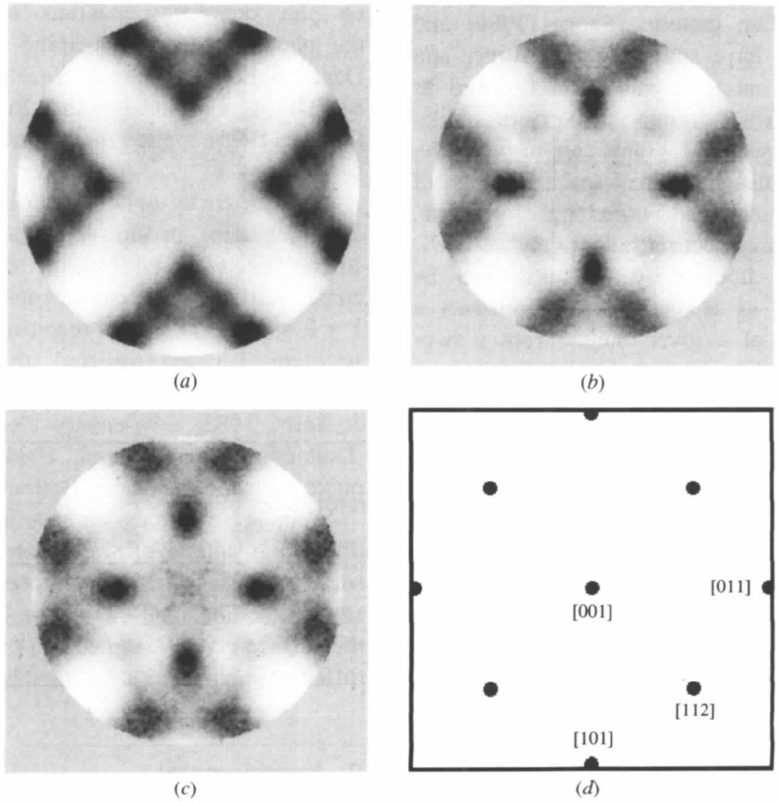

Figure 1
Si 2*p* photoelectron diffraction patterns from an Si(001) surface. The photoelectron kinetic energies are (*a*) 350, (*b*) 450, and (*c*) 650 eV; (*d*) shows the position of crystallographic axes such as [112] and [011] in these patterns.

can derive the orientation of the crystal from these patterns as easily as from LEED patterns. Since the incident angle of the synchrotron radiation is normal to the surface and the photoelectrons are preferentially ejected in the direction of its electric vector, the photoemission in the surface-normal direction is essentially weak. Since the transmittance efficiency pattern is evaluated by azimuthal rotations only, the [001] forward-focusing peak is not observable in the normalized patterns shown in Figs. 1(*a*)–1(*c*). In the central area ($\theta \leq 30°$) of Figs. 1(*a*)–1(*c*) we can see some weaker peaks whose positions appreciably depend on the photoelectron kinetic energy. These peaks are thought to be due to diffraction effects.

4. Analysis

The real-space images $u(\mathbf{r})$ can be obtained by Fourier transformation of the photoelectron diffraction patterns according to the Helmholtz–Kirchhoff integral equation (Barton, 1988),

$$u(\mathbf{r}) = \left| \int \mathrm{d}\mathbf{k}\, \chi(\mathbf{k}) \exp(i\mathbf{k}\cdot\mathbf{r}) \right|. \tag{1}$$

Here, $\chi(\mathbf{k})$ is the photoelectron diffraction pattern, known as the hologram function in the theory of holography, $\mathbf{k}$ is the photoelectron wave vector, $\mathbf{r}$ is the real-space position vector with its origin at the emitter (in Fig. 2, for example, the atom O is at the origin), and $u(\mathbf{r})$ expresses the spatial distribution of scatterers, *i.e.* the real-space atomic position probability. For a constant-kinetic-energy photoelectron diffraction pattern, *i.e.* k constant photoelectron diffraction as we observed, (1) is rewritten as (Barton, 1988):

$$U_k(\mathbf{r}) = \int_{-1}^{1}\int_{-1}^{1} \mathrm{d}K_x \mathrm{d}K_y [\chi(\mathbf{k})/\cos\theta] \times \exp\left\{ ik\left[xK_x + yK_y + z(1 - K_x^2 - K_y^2)^{1/2}\right]\right\}. \tag{2}$$

Here, $U_k(\mathbf{r})$ is the real-space existence probability function, $k = (2mE)^{1/2}/\hbar$, $\mathbf{k} = k\hat{\mathbf{K}} = [kK_x, kK_y, k(1 - K_x^2 - K_y^2)^{1/2}]$ and θ is the polar angle of $\mathbf{k}$. $\mathrm{d}\mathbf{k}$ in (1) has been rewritten as $\mathrm{d}\mathbf{k} = k^2\,\mathrm{d}k\mathrm{d}\Omega = k^2\,\mathrm{d}k(\mathrm{d}K_x\,\mathrm{d}K_y/\cos\theta)$, and we omitted $k^2\mathrm{d}k$ here because k is constant. The integral area is restricted by the condition $1 - K_x^2 - K_y^2 \geq 0$. The kinetic energy E is the sum of the photoelectron kinetic energy E_k and of the inner potential, 12 eV.

The photoelectron wave ψ_0 emitted from the atom O before scattering can be written as

$$\psi_0 = \exp(ikr)/r. \tag{3}$$

The singly scattered wave by the atom j at $\mathbf{R}_j$ can be written as

$$[\exp(ikR_j)/R_j] f_j(\hat{\mathbf{K}}) \exp(ik|\mathbf{r} - \mathbf{R}_j|)/|\mathbf{r} - \mathbf{R}_j| \longrightarrow [\exp(ikR_j)/R_j] f_j(\hat{\mathbf{K}}) \exp[i(kr - \mathbf{k}\cdot\mathbf{R}_j)]/r \tag{4}$$

as $r \to \infty$, where $f_j(\hat{\mathbf{K}})$ is the scattering factor of the jth atom for the direction of $\hat{\mathbf{K}}$. The normalized hologram function $\chi(\mathbf{k})$ is the oscillating part of $|\psi_0 + \psi_1|^2/|\psi_0|^2$, where ψ_1 is the sum of the scattered wave. Using (4), $\chi(\mathbf{k})$ is written as

$$\chi(\mathbf{k}) \simeq \sum_j F_j(\hat{\mathbf{K}}) \exp(ikR_j) \exp(ik\hat{\mathbf{K}}\cdot\mathbf{R}_j) + F_j^*(\hat{\mathbf{K}}) \exp(-ikR_j) \exp(ik\hat{\mathbf{K}}\cdot\mathbf{R}_j), \tag{5}$$

where $F_j(\hat{\mathbf{K}})$ is $f_j(\hat{\mathbf{K}})/R_j$. Equation (5) shows the first-order interference term in the scattering process. If one substitutes (5) into (2) and integrates over the direction of $\hat{\mathbf{K}}$ for various $\mathbf{r}$, one can see peaks in the reconstructed image at the positions $\mathbf{r} = \mathbf{R}_j$ produced by the first term in (5), and at $\mathbf{r} = -\mathbf{R}_j$ by the second term. Hence, in single-energy electron holography, the reconstruction image produces a 'twin image'.

In order to correct this problem we then applied the ES method. This method is based on integration of $U_k(\mathbf{r})$ over absolute values of $\mathbf{k}$ and has the effect of reducing the 'twin image' effect (Barton, 1991). The ES equation is written as

$$u^{\mathrm{ES}}(\mathbf{r}) = \left| \int_{k_{\min}}^{k_{\max}} \mathrm{d}k U_k(\mathbf{r}) \exp(-ik|\mathbf{r}|) \right|. \tag{6}$$

This integration erases the second term in (5) (the 'twin') at $\mathbf{r} = \mathbf{R}_j$ because of the oscillating nature of $\exp(-2ikR_j)$ whereas the first term remains because the phase $\exp[ik(R_j - R_j)]$ does not oscillate. Here, $k_{\max} = 13.17\ \text{Å}^{-1}$ (650 eV), $k_{\min} = 9.741\ \text{Å}^{-1}$ (350 eV), and the integration is replaced by summation for the three energies.

Next, we applied the SWEEP method proposed by Huang *et al.* (1991). This method is based on a Fourier transformation in the small $\mathbf{k}$-space angular window around the real-space $\mathbf{r}$ vector in addition to (4), and has the effect

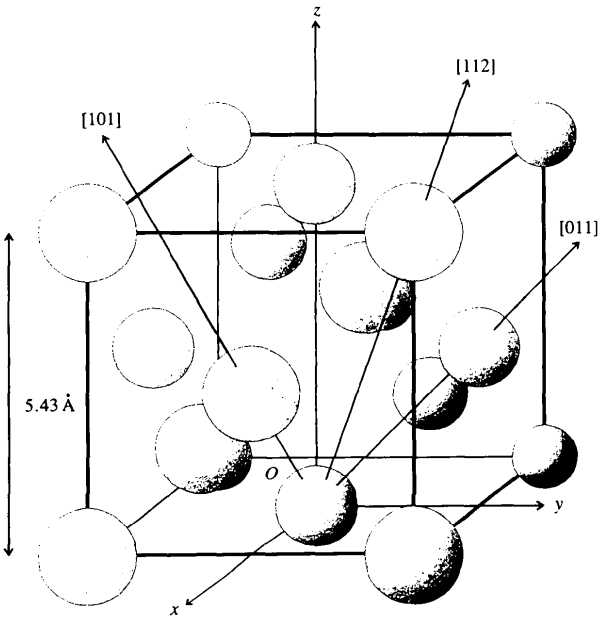

Figure 2
Unit cell of Si.

of reducing the influence of forward-focusing peaks from other atoms. The equation of this method is written as

$$u^{\mathrm{SWEEP}}(\mathbf{r}) = \left| \int_{k_{\min}}^{k_{\max}} \mathrm{d}k\, U_k^{\mathrm{SW}}(\mathbf{r}) \exp\left(-ik|\mathbf{r}|\right) \right|, \qquad (7)$$

where

$$U_k^{\mathrm{SW}}(\mathbf{r}) = \int_{-1}^{1}\int_{-1}^{1} \mathrm{d}K_x \mathrm{d}K_y [\chi(\mathbf{k})\, w(\alpha,\mathbf{K},\hat{\mathbf{r}})/\cos\theta] \times \exp\left\{ ik\left[xK_x + yK_y + z(1 - K_x^2 - K_y^2)^{1/2}\right]\right\} \qquad (8)$$

Here, $w(\alpha,\mathbf{K},\hat{\mathbf{r}})$ is a small-window (SW) function that has a value of unity inside the cones of half angle α (in our case, $\alpha = 20°$) centred at the reconstruction direction $\hat{\mathbf{r}}$, and is zero everywhere else.

The results of all methods are summarized in Figs. 3 and 4. Fig. 3 shows real-space images generated from Fig. 1(*b*) only, *i.e.* produced from the hologram function at $E_k = 450\,\mathrm{eV}$ ($k = 11.01\,\mathrm{Å}^{-1}$). Figs. 3(*a*)–3(*d*) show $|U_k|$ reconstructed from Fig. 1(*b*) by using equation (2). Figs. 3(*e*)–3(*h*) show $|U_k{}^{\mathrm{SW}}(\mathbf{r})|$ reconstructed from the same diffraction pattern by (8). Fig. 4 shows real-space im-

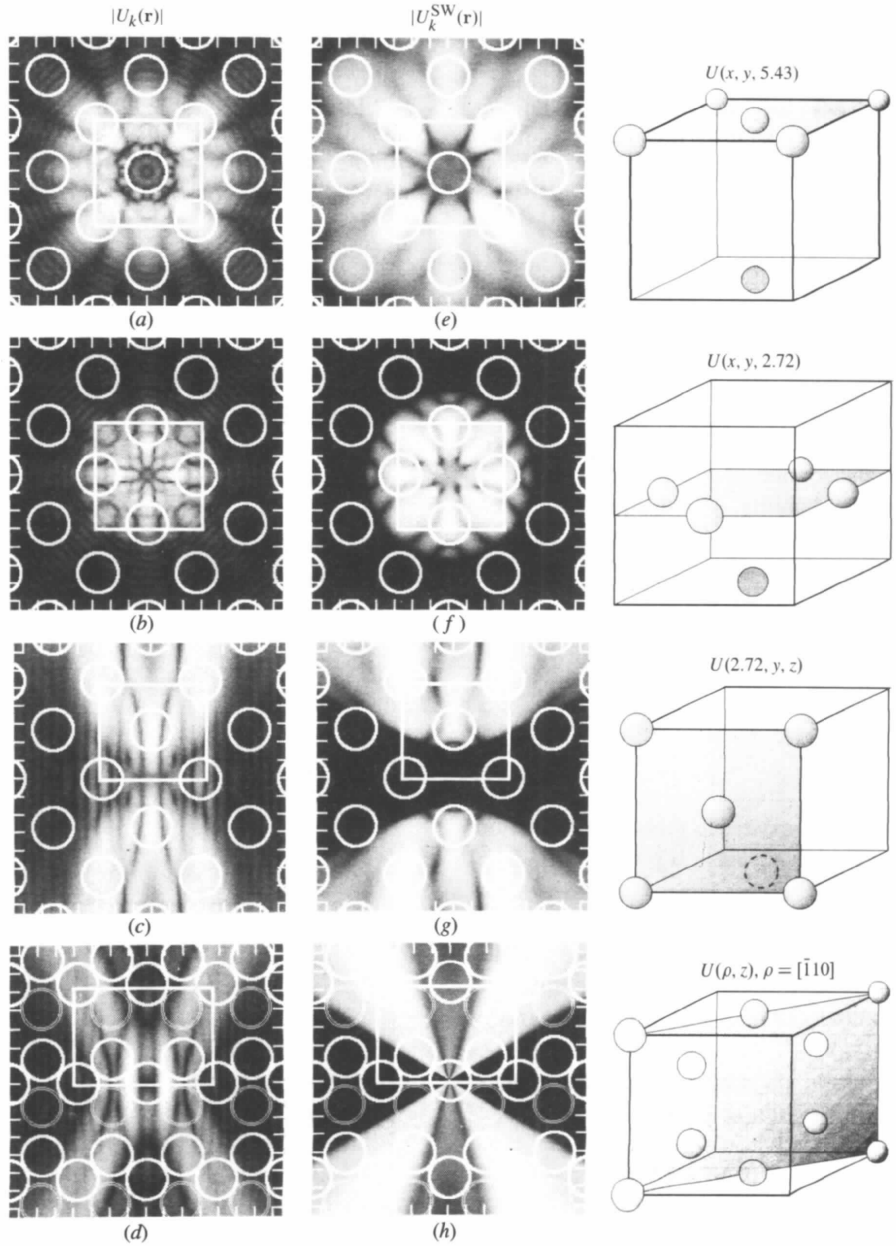

Figure 3
Real-space images reconstructed from the photoelectron diffraction pattern at a kinetic energy of 450 eV (Fig. 1*b*) only. The images (*a*)–(*d*) are $|U_k(\mathbf{r})|$ calculated according to equation (2), and those of (*e*)–(*h*) are $|U_k{}^{\mathrm{SW}}(\mathbf{r})|$ calculated according to equation (6). The planes for which the reconstruction has been made are shown on the right-hand side.

ages generated from Figs. 1(*a*)–1(*c*) by the ES method. Figs. 4(*a*)–4(*d*) show $u^{ES}(\mathbf{r})$ reconstructed using (6), and Figs. 4(*e*)–4(*h*) show $u^{SWEEP}(\mathbf{r})$ reconstructed using (7).

The open circles in Figs. 3 and 4 indicate the position of Si atoms derived from the Si crystal structure; the radius of the circles is the atomic radius of Si (1.17 Å) and the width and height of each panel are both 15 Å. In both Figs. 3 and 4, (*a*) and (*e*) are real-space images of the (001) cross section at 5.43 Å above the emitter, (*b*) and (*f*) are real-space images of the (001) cross section 2.72 Å above the emitter, (*c*) and (*g*) are those of the (100) cross section 2.72 Å from the emitter, and (*d*) and (*h*) are those of the (110) cross section passing through the emitter. On the right-hand side of each image, the corresponding plane is shown in the unit cell. A constant has been subtracted from the hologram function $\chi(\mathbf{k})$ so that its average in the whole area is zero as in Fig. 1; as a consequence, the centre of every real-space image is weak in this analysis. In (*d*) and (*h*) for the (110) cross section, we put circles at (a/4, –a/4, 3a/4), (–a/4, a/4, 3a/4) *etc.* (a is the lattice constant), in addition to (a/4, –a/4, a/4), (–a/4, a/4, a/4) *etc.*, because we must consider that the diffraction pattern is produced

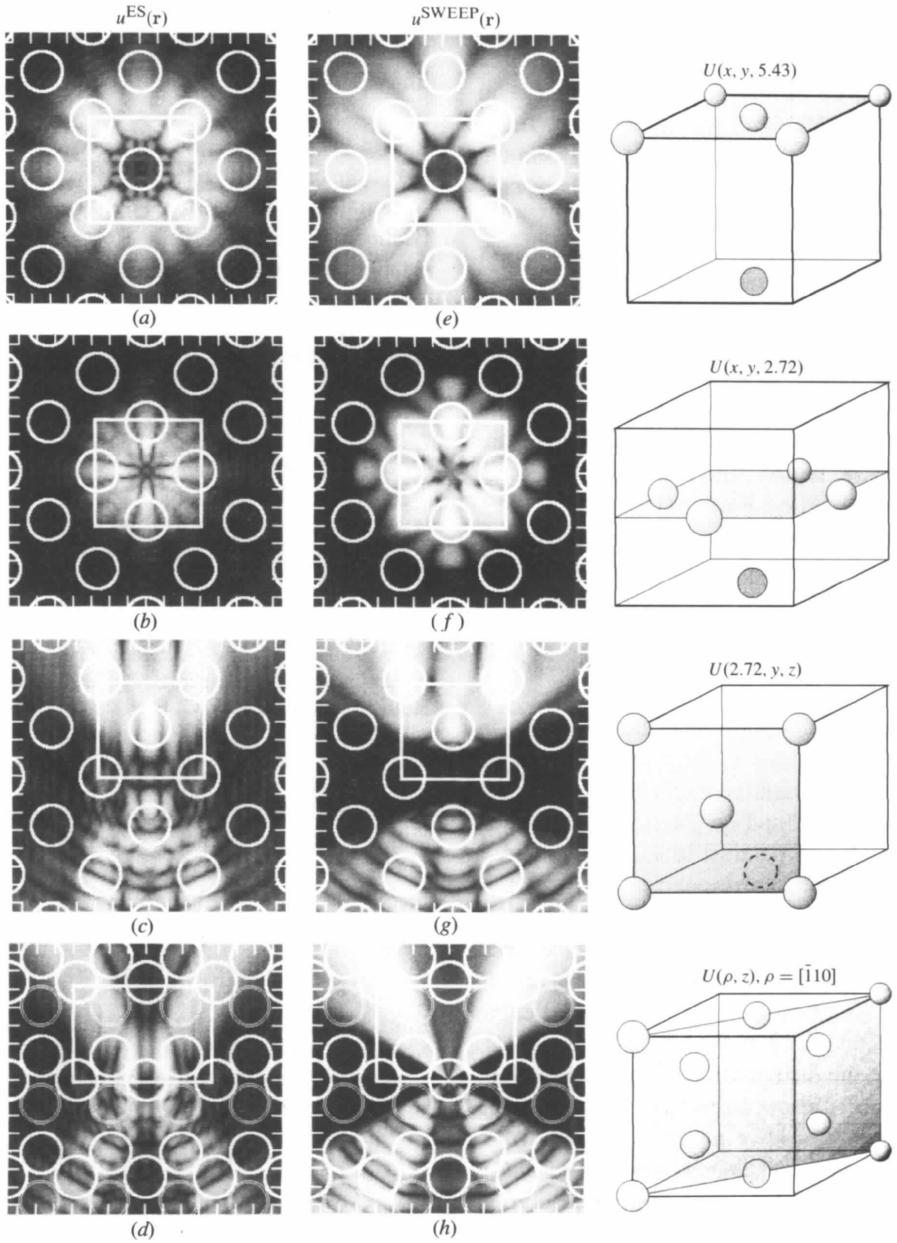

Figure 4
Real-space images reconstructed by using the energy-summation method. The images of (*a*)–(*d*) are $u^{ES}(\mathbf{r})$ calculated according to equation (4), and those of (*e*)–(*h*) are $u^{SWEEP}(\mathbf{r})$ calculated according to equation (5). The shaded planes on the right-hand side are the same as in Fig. 3.

by the photoelectrons from the atoms not only at the origin (0, 0, 0) but also at ($a/4$, $-a/4$, $a/4$).

5. Discussion

In the single-energy full-window method, the peak positions reconstructed in Figs. 3(*a*) and 3(*b*) deviate by *ca* 1 Å to the centre of the image from the position expected from the Si crystal structure. In Figs. 3(*c*) and 3(*d*) most peaks are prolonged in the vertical direction possibly because of the limited polar detection angle (0–47° in this experiment) which will be discussed below.

In the single-energy small-window method the peak positions in Figs. 3(*e*) and 3(*f*) better reproduce the Si crystal structure, although the form of the reconstructed peaks is much broader than those of the previous method, possibly as a result of the condition that the integral area is restricted by $w(\alpha, \mathbf{K}, \hat{\mathbf{r}})$. Strong peaks are noticeable in the positions where no circles are drawn in Fig. 3(*f*). These peaks may originate from the tails of the strong peaks in the [112] direction *etc.*, as suggested in Fig. 3(*h*) where tails are visible at z = 2.72 Å.

The ES method has the effect of enhancing the peaks in the actual atomic position whereas the spurious peaks are reduced. The atomic positions, however, deviate considerably from the correct positions (compare Fig. 3 with Fig. 4). One possible reason is that only three patterns at different E_k are used here. The most prominent feature in the energy-summed images is that the twin images are strongly suppressed in the region with negative z (Figs. 4*c*, 4*d*, 4*g* and 4*h*), as discussed by Barton (1991).

As far as the lateral atomic geometry is concerned, the small-window method gives better results than the full-angle integration method. The deviations of the peak positions in Figs. 4(*e*) and 4(*f*) from the expected positions are smaller than those of the full-window images of Figs. 4(*a*) and 4(*b*).

The results in Figs. 3 and 4 show that the resolution in the z direction is worse than those in the x and y directions. We believe that this result should be expected, because the region of the experimental diffraction patterns in **k** space is only $7.51 \leq k_z \leq 11.01$ Å^{-1} in contrast to $|k_x, k_y| \leq 8.05$ Å^{-1} for E_k = 450 eV. These results correspond to $\Delta z \simeq 2.15$ Å whereas Δx, $\Delta y \simeq 0.47$ Å (Tong, Li & Huang, 1991).

Even in Figs. 4(*d*) and 4(*h*) the peaks are prolonged in the [112] direction. In order to understand such results we must note that the Si lattice has two face-centred cubic sublattices, one originating at (0, 0, 0) and the other at (1/4, 1/4, 1/4). Accordingly, the diffraction patterns contain both contributions. Therefore, the reconstructed images in the (110) cross section appear to have peaks at not only ($a/4$, $-a/4$, $a/4$), ($-a/4$, $a/4$, $a/4$) but also at ($a/4$, $-a/4$, $3a/4$), ($-a/4$, $a/4$, $3a/4$). This is another cause of poor resolution in this plane.

6. Conclusions

We have measured photoelectron diffraction patterns from the Si(001) surface at three photoelectron kinetic energies (350, 450 and 650 eV). We have tested the major methods of photoelectron holography, such as a simple Fourier transformation, the small-window method, the energy-summation method and the SWEEP method, to obtain real-space images in the (001), (100) and (110) planes. Without taking into account the atomic scattering factor as in the case of SWIFT, we have obtained clear real-space images in the cross section parallel to the surface with the SWEEP method. In the cross section perpendicular to the surface we cannot obtain good real-space images with high resolution because of the limited range of k_z in this experiment. By taking data over a wider range of k_z, we should be able to obtain higher resolution real-space images even in this cross section.

The authors are grateful to the staff of the synchrotron radiation facility of KEK. The work was supported by the National Laboratory for High Energy Physics and by a Grant-in-Aid for Scientific Research from the Ministry of Education, Science, Culture and Sports in Japan.

References

Barton, J. J. (1988). *Phys. Rev. Lett.* **61**, 1356–1359.
Barton, J. J. (1991). *Phys. Rev. Lett.* **67**, 3106–3109.
Bullock, E. L., Gunnella, R., Patthey, L., Abukawa, T., Kono, S., Natoli, C. R. & Johansson, L. S. O. (1995). *Phys. Rev. Lett.* **74**, 2756–2759.
Daimon, H. (1988). *Rev. Sci. Instrum.* **59**, 545–549.
Daimon, H. (1990). *Rev. Sci. Instrum.* **61**, 205.
Denecke, R., Eckstein, R., Ley, L., Bocquet, A. E. & Leckey, R. C. G. (1995). *Surf. Sci.* **331/333**, 1085–1092.
Gabor, J. (1948). *Nature (London)*, **161**, 777.
Hardcastle, S., Han, Z.-L., Harp, G. R., Zhang, J., Chen, B. L., Saldin, D. K. & Tonner, B. P. (1991). *Surf. Sci.* **245**, L190–194.
Holland, B. W., Duke, C. B. & Paton, A. (1984). *Surf. Sci. Lett.* **140**, L269–278.
Huang, H., Li, H. & Tong, S. Y. (1991). *Phys. Rev. B*, **44**, 3240–3245.
Namba, H., Daimon, H., Idei, Y., Kuroda, H., Taniguchi, M., Suga, S., Murata, Y., Ueyama, K. & Miyahara, T. (1989). *Rev. Sci. Instrum.* **60**, 1909–1912.
Nishimoto, H., Daimon, H., Suga, S., Tezuka, Y., Ino, S., Kato, I., Zenitani, F. & Soezima, H. (1993). *Rev. Sci. Instrum.* **64**, 2857–2862.
Roesler, J. M., Sieger, M. T., Miller, T. & Chiang, T.-C. (1995). *Surf. Sci. Lett.* **329**, L588–592.
Rous, P. J. & Rubin, M. H. (1994). *Surf. Sci.* **316**, L1068–1074.
Szöke, A. (1986). *Short Wavelength Coherent Radiation: Generation and Applications*, AIP Conference Proceedings No. 147, edited by D. T. Attwood & J. Boker. New York: American Institute of Physics.
Tong, S. Y., Li, H. & Huang, H. (1991). *Phys. Rev. Lett.* **67**, 3102–3105.
Tromp, R. M., Smeenk, R. G. & Saris, F. W. (1983). *Surf. Sci.* **133**, 137–158.